ADVANCED PHOTONICS RESEARCH
Open Access
www.adpr-journal.com

Zirconium Nitride: Optical Properties of an Emerging Intermetallic for Plasmonic Applications

Alireza Shabani, Matiyas Tsegay Korsa, Søren Petersen, Mehdi Khazaei Nezhad, Yogendra Kumar Mishra, and Jost Adam**

Finding new plasmonic materials with prominent optical properties and unique physical and chemical characteristics, which are merits of traditional gold and silver, is of great interest to many applications. This work uses a series of powerful numerical methods, such as density functional theory (DFT) and electromagnetic modeling approaches, to predict the plasmonic response of a mechanically well-known material, zirconium nitride (ZrN). DFT first delivers an electronic analysis and optical dispersion data between 1 and 8 eV, experimentally verified in the lower energy regime ($<$ 4 eV), and extremely valuable for any subsequent optical modeling. Subsequent electromagnetic modeling steps, including the transfer matrix method (TMM) and Mie theory, demonstrate the excitation of surface plasmon polaritons and localized surface plasmon resonances in ZrN thin films and nanoparticles. Furthermore, the finite-difference time-domain (FDTD) method exhibits the excitation of distinct electric (plasmon) and magnetic (LC) resonances in a periodic array of u-shaped ZrN split-ring resonators (SRRs). The findings showcase an optical behavior comparable with structures made from noble metals such as gold and silver and support the introduction of ZrN as a new and appropriate candidate for plasmonic applications, specifically in technological applications where optical and mechanical properties are of simultaneous concern.

1. Introduction

The efforts to reach out to new, cost-effective, and robust plasmonic materials, possessing extraordinary optical properties, and meeting the required conditions of various applications, are getting extensively important concerning future technological requirements. Although the most often used noble metals, such as gold (Au) and silver (Ag), demonstrate a strong optical response in plasmonic and metamaterial applications (at the visible spectrum), some of their inherent features, such as a high rate of interband losses in the visible spectrum,[1,2] lack of compatibility with standard silicon devices due to the large magnitude of the real part of the dielectric function,[3,4] low thermal stability at high temperatures, relatively quick degradation in air,[5,6] and, the most crucial factor, lack of achievable tunable optical properties,[7] render them less suitable for real-world applications. To tackle this problem, the community is intensely focusing on material characteristics through the response functions such as optical permittivity and refractive indices, where someone could find all the required information about optical behavior and readily evaluate the plasmon efficiency of the candidate materials. As a general rule, the metallic characteristic, which is the origin of plasmon phenomena, occurs for the frequencies at which the real part of the dielectric function is negative. At the same time, to favor large propagation lengths and thereby high resonance Q-factors, a plasmonic material ideally possesses a low rate of optical loss, which is specified by the imaginary part of dielectric function (ε).[8–10] It requires a low plasmon frequency (ω_p) as well as low damping factor (γ) value according to the Drude–Lorentz model describing optical properties of materials.[1,2] The first is directly associated with the number of free electrons in a metal, whereas the second indicates the degree of order in the crystal structure.

Based on this, different material classes were introduced as alternatives for noble metals in plasmonics and metamaterials. Generally speaking, we can categorize them into two subsets based on the free charge carrier population directly influencing the metallic features of a plasmonic material. In the first group, a reduction in the number of free electrons in the metallic element occurs through bonding it to a nonmetal element, giving rise to a

A. Shabani, M. Tsegay Korsa, S. Petersen, J. Adam
Computational Materials Group
Department of Mechanical and Electrical Engineering
University of Southern Denmark
DK-6400 Sønderborg, Denmark
E-mail: shabani@sdu.dk; jostadam@sdu.dk

M. Khazaei Nezhad
Department of Physics
Faculty of Science
Ferdowsi University of Mashhad
Mashhad 9177948974, Iran

Y. Kumar Mishra
Smart Materials, NanoSYD
Mads Clausen Institute
University of Southern Denmark
DK-6400 Sønderborg, Denmark

The ORCID identification number(s) for the author(s) of this article can be found under https://doi.org/10.1002/adpr.202100178.

DOI: 10.1002/adpr.202100178

decrease in plasmon frequency and optical loss. Transition metal nitrides belong to this category. In the second group, a metallic dopant is introduced to a semiconductor to change the electronic properties and inject more free electrons into the system. This behavior was seen in transparent conducting oxide (TCO) family, especially in the cases of Al/Ga-doped zinc oxide.[11–15] The maximum performance of each family is limited to a particular spectral region. For instance, TCOs exhibit plasmonic behavior in the near-infrared (NIR) regime, due to the low carrier concentration and subsequently small ω_p, whereas nitrides have the optical properties similar to the Ag and Au with plasmonic behavior at visible region.[1,2] Nitrides are nonstoichiometric compounds with good electrical conductivity comprising metallic properties in the visible and for longer wavelengths. They are known as hard materials with high melting points and refractory properties (chemically stable at high temperatures), possessing the potential of easy fabrication and integration with standard silicon manufacturing processes.[16–18] One of the advantages of nitrides is their capability to tailor the electronic properties by varying their composition, not observed in traditional metals. Among nitrides, TiN is of great interest to researchers and extensive studies have been done about its structural, optical, and electronic behavior.[19–22] Another member of the nitrides family, ZrN, has gained little attention, as only a few reports concern its optical properties; however, it is also a binary intermetallic compound showing similar features to TiN and exhibiting a gold-colored appearance.[23–26] Motivated by the aforementioned, we intend to investigate the optical response of ZrN in several well-known geometries and evaluate its plasmonics performance in such structures.

Here, using first-principles calculations (density functional theory [DFT]), combined with three different electromagnetic (EM) modeling approaches, including transfer matrix method (TMM), Mie scattering, and finite-difference time-domain (FDTD), we investigate the optical response of ZrN in various plasmonic geometries. More specifically, after calculating the structural, electronic, and optical properties of ZrN via DFT, we extract the calculated ZrN's dispersion functions, n and k, to use in the Kretschmann angle configuration via TMM as well as nanoparticle scattering via Mie theory, showing the ZrN's capability in exciting the surface plasmon polariton (SPP) and localized surface plasmon (LSP) resonances. We also apply the Drude–Lorentz model on the imaginary part of the dielectric function to introduce ZrN into the FDTD method for further metamaterial simulations through a 2D array of split-ring resonators (SRRs) made of intermetallic ZrN. We provide essential material data and modeling recipes in the interdisciplinary field between solid-state physics and optics. This study is not only the first and most comprehensive demonstration of the plasmonic capability of ZrN in the well-known plasmonic configurations, showing a remarkable plasmonic response in the optical spectrum, comparable with the most used Au and Ag, but also showcases the applicability and details of our proposed method in predicting light–matter interaction of a system from atomic building blocks to micro/nanoscopic structures. The here presented detailed investigations about optical properties of ZrN-based nanoparticles, thin films, and metamaterials will facilitate the development of future advanced optoelectronic devices.

2. Results and Discussions

The atomic arrangement of any material is the most important parameter deciding its physical properties. We performed a full DFT-based structural optimization for the ZrN material (see Computational Methods for details; **Table 1** includes the calculated lattice parameters). The relaxed lattice parameter is $a = 4.60$ nm, in good agreement with experimental and theoretical reports.[27–29]

With Rocksalt crystal structure (**Figure 1**a), ZrN exhibits the space group of Fm3m, and it can be described as two face-centered cubic lattices of metal (Zr) and nonmetal (N), moved in the size of half of the main diameter with respect to each other, or as a metal cubic close-packed structure with all octahedral voids occupied by nonmetal.

2.1. Density of States and Electric Permittivity

Due to the close association between electronic and optical material properties, we show the electronic densities of states (DOS) as well as optical dielectric function of ZrN in **Figure 2**.

The procedure of extracting the DOS and the electric permittivity from DFT calculations is similar to the one recently demonstrated by the authors for aluminum-doped zinc oxide (AZO), a member of the TCO family.[30] The chemical bonding in ZrN stems from the hybridization of N 2*p* with Zr 3 *d* electrons. Also, the conductivity feature of ZrN is due to the partially filled Zr 4 *d* state, which intersects the Fermi energy. We can categorize the occupied states below the Fermi level in two main energy regions: from -8 to -2.5 eV, in which a strong hybridization of the *d* electrons of Zr with the *p* electrons of N occurs, which is the origin of interband transitions in dielectric function, as well as the region exactly located below the Fermi level at energy rang of -2.5 to 0 eV, which we attribute to the Zr 4*d* state with a small contribution of the N 2*p* state (near zero contribution). Based on the selection rule ($\Delta = 0, \pm 1$) and hybridization between N and Zr, the electron interband transitions occur from N *p* to Zr *d* states. Consequently, there exists a threshold in the imaginary part of the dielectric function (at the energy of 2.5 eV) due to the near-zero value of the N *p* state in the second region of DOS. Also, we attribute the peaks indicated by arrows in the imaginary part of the dielectric function to the electron transitions from the shoulder and peak of DOS, located at around -3.5 and -5 eV, to the empty states above Fermi level. We have demonstrated these two energies by E_{01} and E_{02} in Figure 2a. The present results for the DOS of ZrN agree with other reports, indicating the reliability of our calculations.

Table 1. The optimized structural parameters of ZrN in the Rocksalt crystal structure with GGA pseudopotential.

	Present	Exp. and cal.
a [Å]	4.6	4.57[27]
		4.60[28]
		4.57[29]
$\alpha = \beta = (\gamma)$ [°C]	90	90
V [Å^3]	97.85	–

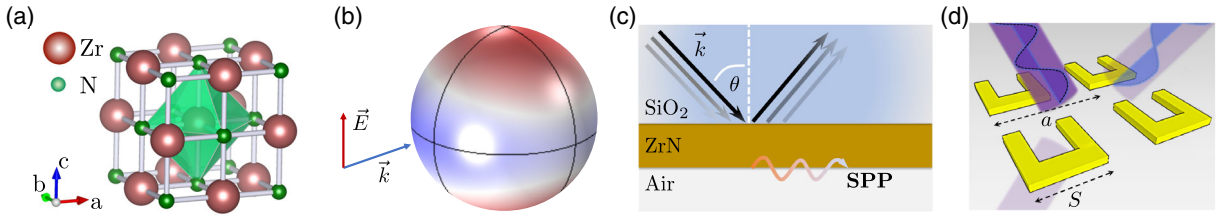

Figure 1. a–d) This work investigates the potential of ZrN for plasmonic applications, from the atomic scale to metamaterial application. a) Rocksalt crystal structure of ZrN in polyhedral representation; b) numerical setup of ZrN particle scattering investigations ($\vec{k}$ and $\vec{E}$ indicate the incident wave direction and electric field polarization, respectively); c) numerical setup of ZrN thin-film investigations (θ represents the incidence angle with respect to the ZrN surface normal); d) schematic of the proposed SRR system including a square array of four u-shaped ZrN's SRRs (*a* and *S* indicate the periodic lattice constant and size of resonators, respectively).

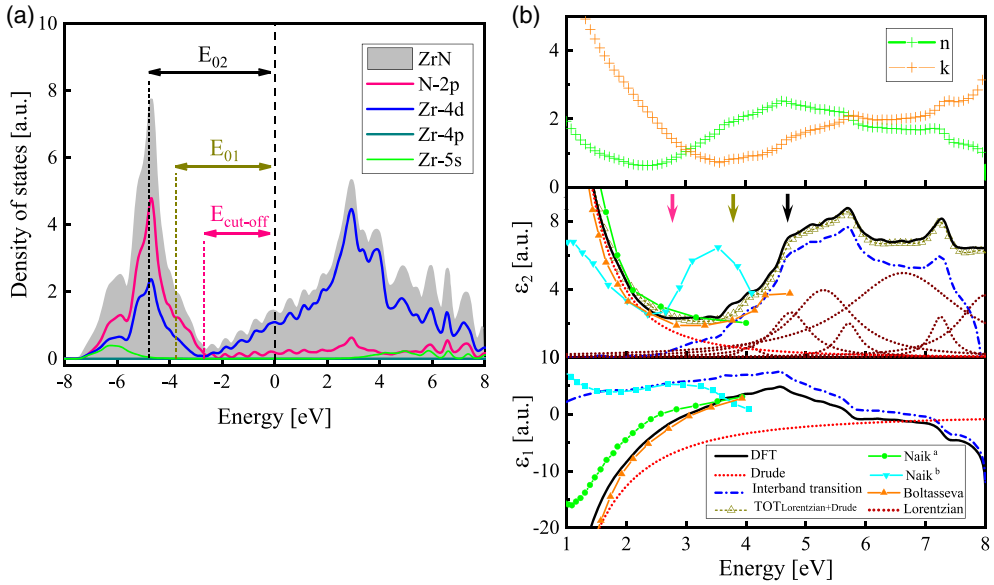

Figure 2. Electrical and optical dispersion data calculated by DFT with GGA pseudopotential: a) total and partial DOS of ZrN. The Fermi energy was set at zero; b) upper row: calculated real (*n*) and imaginary (*k*) parts ZrN's refractive index, for energies up to 8 eV. Lower two rows: calculated real and imaginary parts of the dielectric function (solid black line). The sum over all Lorentzian peaks (dotted brown lines) and the Drude term (dotted red line), represented by "TOTLorentzian+Drude" legend, matches well with DFT results. The experimental data (available up to ≈ 4eV) were taken from the literature (Boltasseva,[7] Naika,b[9]).

It is worth mentioning that although the interband transitions also exist in nonmetallic dispersive materials, such as insulators and semiconductors, they have a crucial role in metals by manipulating the screening of unbound electrons, which leads to the alteration of plasmon and crossover frequencies and subsequently to metallic regions. For the low energy regime (near zero) in the ε curve of Figure 2b, the intraband transition mechanism appears, which is modeled by the Drude equation, and it indicates the metallic characteristics for ZrN. Therefore, this region is of great importance for pursuing plasmonic properties. We have used the Drude damping coefficient of 0.62 eV, taken from Kim et al.,[23] as an empirical parameter to depict the intraband transition contribution. This coefficient represents the loss rate of conduction electrons passing through the crystal of metals via defect scattering mechanisms, lattice vibrations, and surface states. Furthermore, Figure 2b compares our results for the real and imaginary of ε with experimental data available in the literature[7,9] for the low energy region (1–4 eV). As one can see, the DFT-based curves match with Boltasseva experimental results, as the main characteristics of dielectric permittivity, including intra- and interband transitions and absorption edge, occur approximately in the same energies for our calculations and the experiment, indicating the validity of our DFT calculations, whereas Naik results are a bit different, which may be due to utilizing different experimental techniques. These optical dispersion data extend till 8 eV, which we consider interesting for upcoming modeling approaches in the low wavelength regime: the negative ε_1 values beyond 5.5 eV imply potential metallic behavior for plasmonic purposes. This study will only focus on the midranged wavelengths, where there are attractive applications for optical devices.

With a negative real part of dielectric function for ZrN, exhibiting metallic behavior in the visible and longer wavelengths, and a comparable interband loss to TiN as the most studied case of

nitrides family, ZrN shows the potential of being used in plasmonic and metamaterial structures. To this end, we applied the Drude–Lorentz model (Equation (1)) to the imaginary part of the dielectric function calculated by DFT to extract the optical quantities required for further EM simulations.[31] Both classical and quantum mechanics views of electron transitions in material, including intraband and interband transitions of free and bound electrons, are considered in this model

$$\varepsilon(\omega) = \varepsilon_{\infty}(\omega) + \sum_{j} \frac{f_j \omega_{\mathrm{p}}^2}{(\omega_j^2 - \omega^2) - i\omega\gamma_j} \tag{1}$$

where ω_j, γ_j, and f_j are the resonance frequency, the damping coefficient, and the resonance strength, respectively. The background permittivity is denoted by ε_{∞}, ω_{p} is the plasma frequency, and ω is the frequency of the incident beam. In this model, each peak in the imaginary part of the dielectric function acts as an oscillator, absorbing the EM wave through a resonance mechanism.

Figure 2b shows the imaginary part of the dielectric function of ZrN fitted by nine Lorentzian distributions. We extracted the parameters of the Drude–Lorentz model by using a plasmon frequency of 7.456 eV, directly obtained from the DFT calculations, as well as a damping coefficient of 0.62 eV.[23] The damping coefficient of each resonance equals the full width at half maximum (FWHM), and the resonance strength stems from the fact that at a resonance frequency, the magnitude of a fitted Lorentzian distribution (amount of peak) should be approximately the same as the corresponding imaginary part of the dielectric function. **Table 2** shows the corresponding results. The first resonance corresponds to the leftmost peak in ε_2 and indicates the Drude model, which specifies the metallic behavior for ZrN and is the origin of plasmonic properties in the following simulations. Other terms in Table 2 are related to interband transitions appearing in higher energies in ε_2. Therefore, we possess all required parameters for embedding ZrN into any EM modeling software/code to study its impact when used as a plasmonic geometry constituent material. Alongside this article, we provide the refractive index and the dielectric function data in the Supporting Information.

Table 2. The optical parameters of Drude–Lorentz model for ZrN obtained from DFT–GGA calculations.

Resonance j	ω_j [eV]	γ_j [eV]	f_j
1	0	0.62	1
2	0.18	0.24	0.03
3	4.06	0.35	0.02
4	4.75	0.76	0.17
5	5.29	1.26	0.48
6	5.72	0.45	0.09
7	6.62	2.27	1.34
8	7.25	0.40	0.12
9	8.01	1.05	0.55

2.2. Optical Behavior of ZrN Particles

To showcase the EM scattering and localized surface plasmon resonance (LSPR) behavior of ZrN particles, we simulated the absorption/scattering efficiency of spherical ZrN nanoparticles in air ($n = 1$, $k = 0$), in the near-visible light spectrum, for various particle diameters (**Figure 3**, upper row). We calculated the efficiency data using an in-house Mie theory[32] code, using the real and imaginary part of the ZrN material refractive index (Figure 1). A prominent peak of absorption/scattering efficiency appears between $\lambda = 650$ and 700 nm, with a minor peak near $\lambda = 300$ nm. This prominent peak corresponds to LSPR of ZrN nanospheres, stemming from oscillating free electron carriers coupled to an incident EM wave. Similar to another member of the transition metal nitride family, titanium nitride (TiN), the plasmonic peak appearance of ZrN also lies within the visible region.[33] The minor peak at lower wavelengths arises due to higher order plasmon modes, which we address to the interband transition peaks in the ε_2 plot (Figure 1), more visible in the scattering cross-section diagram. In this regime, the interband transition mechanism absorbs the incident beam's energy and randomly reemits secondary EM waves in different directions, giving rise to an increase in the scattering cross section. Moreover, the efficiency's magnitude is more substantial at larger particle diameters and slightly redshifts compared with smaller diameter particles. The oscillation's effective length of electrons rises as the LSPRs go to higher wavelengths by increasing the size of nanoparticles.

We compare the optical ZrN particle dispersion to the one of Au particles, reproducing the Mie simulation with the same parameters except for the particle material model changed to Au.[34] For the sake of brevity, we limit our calculations to spherical geometry. Lalisse et al.[35] present a comparative study of Au and ZrN/TiN-based ellipsoid structures, however, purely based on the literature material data.

Figure 3 shows the results of the Au simulation in the lower row. Both setups' behaviors have similar characteristics, i.e., both materials have two peaks for scattering and absorption, and the peak magnitudes decrease with decreasing particle diameter. While the scattering and absorption magnitudes are similar for ZrN and Au, Au comprises significantly sharper peaks at a given particle diameter. Furthermore, both absorption and scattering peaks are blueshifted for the ZrN particles compared with those made of Au. Comparing the plots in Figure 3, one observes that both the scattering and absorption peaks are higher and broader for Au in the low-wavelength regime than ZrN, which we address to the higher and broader interband transitions in Au compared with ZrN.

2.3. Optical Behavior of ZrN Thin Films

To demonstrate the existence of SPPs at the interface between ZrN thin films and a dielectric, we calculate the optical response of a 50 nm-thick ZrN layer, sandwiched between silicon dioxide (SiO_2) and air (Figure 1c). We used an in-house TMM code for multilayer thin films (see the Computational Methods section for details).[36] We excited the structure in the so-called Kretschmann configuration, widely used for the surface plasmon resonance

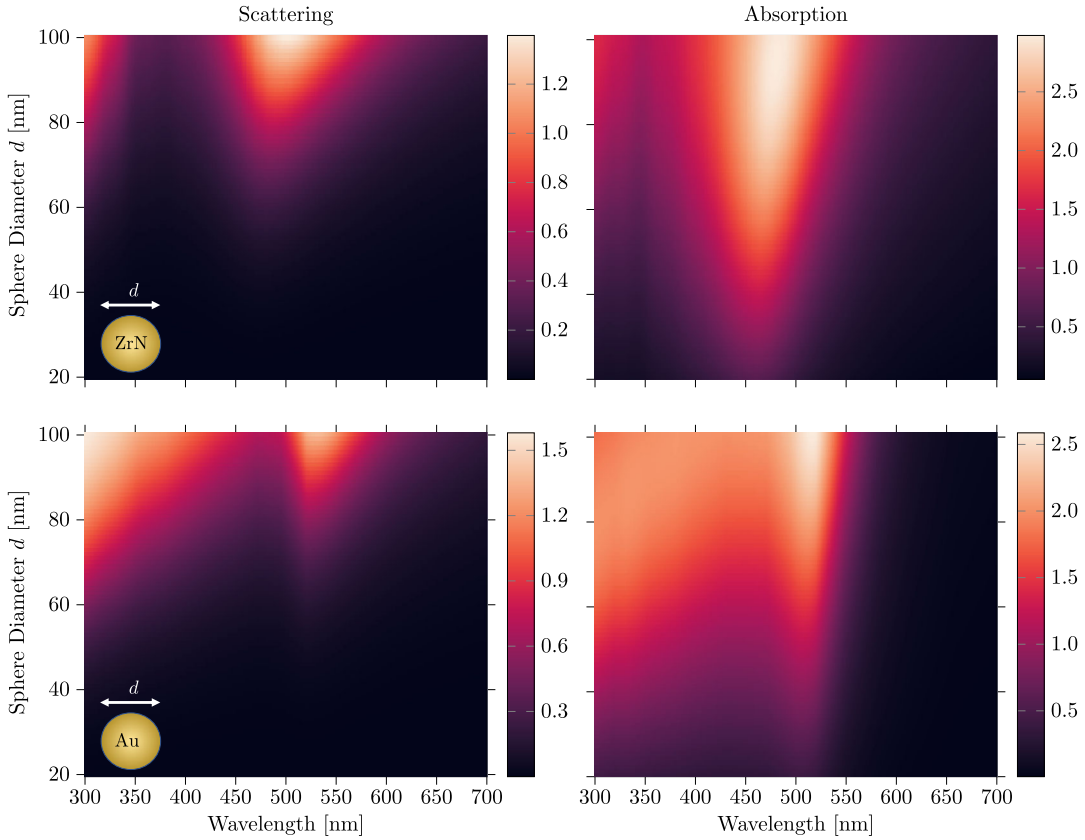

Figure 3. Optical absorption and scattering cross section of a ZrN (upper row) and Au (lower row) nanoparticle, calculated by Mie theory, for varying particle diameters.

detection, with a plane wave incident through SiO_2 under a certain incident angle, potentially creating a surface plasmon resonance at the interfaces between ZrN and the adjacent dielectrics (predominantly at the air–ZrN interface).[37] **Figure 4** shows the ZrN reflection and absorption heat maps, in comparison with the same setup with an Au layer. In this figure, a sharp vertical kink at around 41 °C for both ZrN and Au corresponds to the total internal reflection angle on the interface between the glass and Au/ZrN, if one only considers the real parts of the materials' refractive indices: the reflection rises to 100% for wavelengths beyond 500 nm, and then, for higher angles, starts dropping toward the plasmonic dip at the Kretschmann angle (due to the nonvanishing imaginary part of the refractive indices).

The Kretschmann angle for both stacks corresponds to the minimum reflection path (dark, curved) in the reflection heat maps, in the region 500–800 nm. The region of losses in the absorption heat map confirms the plasmonic resonance at the minimum reflection region. The point of minimum refection varies for different incident angles because the Kretschmann angle θ_{SPR} depends on the metallic films' refractive index n_{met}, which, in turn, depends on the incident wavelength λ (Figure 1, upper row)[38]

$$\theta_{SPR}(\lambda) = \sin^{-1}\left(\frac{1}{n_{inc}\sqrt{n_{ana}^2 n_{met}(\lambda)^2/(n_{ana}^2 + n_{met}(\lambda)^2)}}\right) \quad (2)$$

where n_{ana} and n_{inc} further denote the (constant) refractive indices of the analyte region (here: air) and the region of incidence (here: SiO_2), respectively. Consequently, for varying incident wavelength, the Kretschmann angle varies from 42 to 50 °C for Au and 43 to 50 °C for ZrN.

Comparing the two materials, we observe that the calculated Kretschmann angle (according to Equation (2); see also Figure S1, Supporting Information) is similar for both ZrN and Au films, confirming a similar peak shifting performance in sensing applications (angular or spectral resonance peak shift upon a change of n_{ana}; see Figure S2, Supporting Information). The heat map, however, reveals that the ZrN resonances are softer, e.g., the actual peak shift might be harder to detect in sensing applications.

2.4. ZrN in Plasmonic Metamaterials

We simulated the optical transmission response of a periodic unit cell containing u-shaped SRRs made of ZrN, in a square array (Figure 1d), using the FDTD method (see Computational Methods section for details). **Figure 5** shows the FDTD-calculated optical transmission spectrum of u-shaped ZrN SRRs for different sizes of resonators, ranging from $S = 80$ to 105 nm, and an EM plane wave impinging perpendicularly to the SRR plane. The transmission response strongly depends on

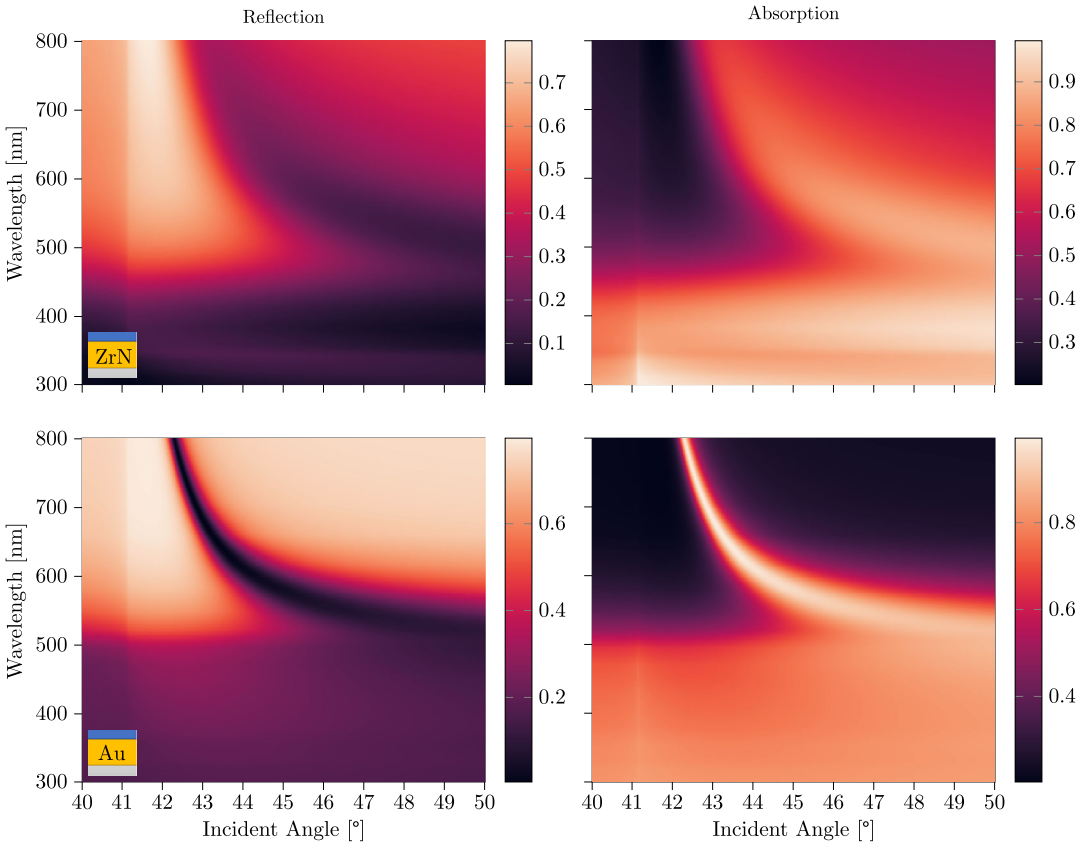

Figure 4. Calculated transfer matrix method reflection and absorption efficiencies for a 50 nm ZrN (upper row) and Au (lower row) thin film, sandwiched between silicon dioxide (SiO_2; $n = 1.52$) and air ($n = 1$). A polychromatic plane wave is incident through the SiO_2 region, polarized within the plane of incidence (TM).

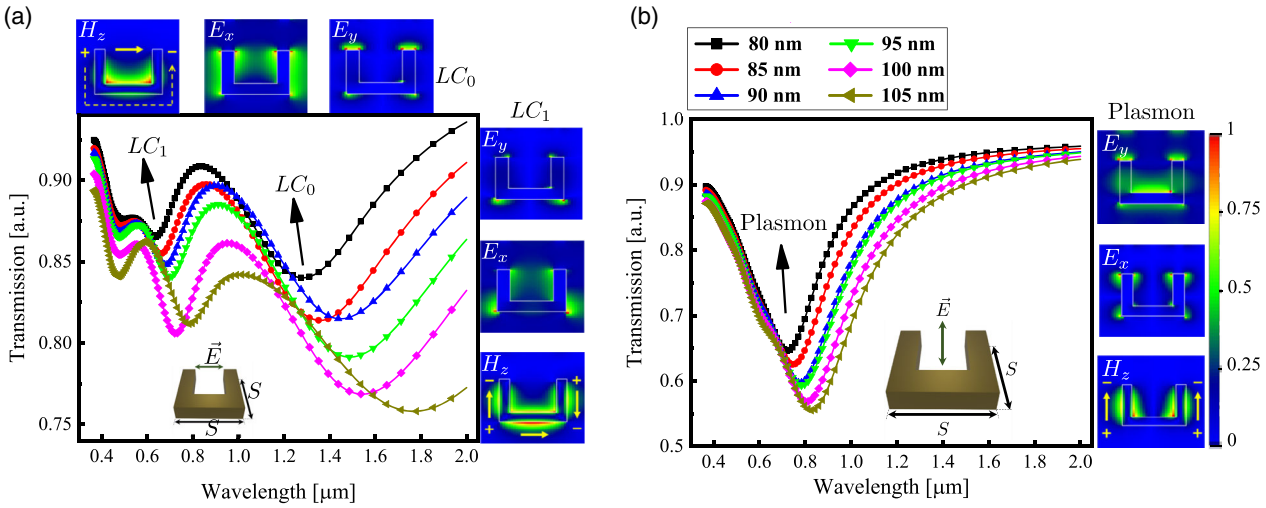

Figure 5. Calculated optical transmission spectra of the proposed ZrN SRR system for a a) TE-polarized (perpendicular to the SRR gap) and b) TM-polarized (parallel to the SRR gap) incident EM wave, for varying resonator sizes *S*. E_x, E_y, and H_z denote the EM field magnitudes relative to the input field magnitude, for the corresponding modes. Yellow solid and dashed arrows indicate electric dipole moment and induced circulating current, respectively. The green arrows indicate the incident wave's electrical polarization.

the incident beam polarization. Two resonances occur for the resonators and an electric field polarization perpendicular to the SRR gap (TE). For a 100 nm-sized resonator, the resonances are located at the wavelengths $\lambda = 720$ and 1540 nm. They are known as the two lowest order magnetic modes excited in the SRR system.[39–41] In the lower energy excited magnetic resonance, $\lambda = 1540$ nm, the coupling between the oscillating electric field and the vertical resonator arms results in an electric dipole moment at the gap region among the vertical arms' tips. It leads to a circulating current in the SRR and, subsequently, to a magnetic dipole moment normal to the SRR plane, stemming from the creation of opposite charges at the tips.

On the contrary, we can also model the magnetic modes by a replaced LC circuit to qualitatively analyze their optical response.[42,43] In this case, the gap region between two vertical arms determines the capacitance behavior, and the three SRR edges play the role of an inductance. Therefore, we can ascribe the zeroth and first orders of LC resonances to the two lowest excited magnetic SRR modes LC_0 and LC_1, respectively (Figure 5a). The inset in Figure 5a also exhibits the calculated EM field component magnitudes E_x, E_y, and H_z, on the surface of 100 nm-sized SRRs, at wavelengths $\lambda = 720$ and 1540 nm, where the LC_1 and LC_0 were excited, respectively. The hot spots in the E_x and E_y profiles, concentrated on the vertical arm tips, confirm the existence of accumulated opposite charges and, therefore, the formation of the electric dipole moment in the gap region (LC_0 mode). The H_z profile also implies an induced magnetic dipole moment normal to the SRR plane due to a circulating current produced by electric dipole moment. In the LC_1 mode, the H_z field was excited in a delocalized form (out of SRR plane) and disturbed on all three SRR parts, stemming from a broken symmetry induced by the antiparallel electric dipole moments in the side arms.

In the case of an incident beam *E*-field polarization parallel to the gap (TM), a single resonance occurs at $\lambda = 810$ nm wavelength for 100 nm-sized ZrN SRRs (Figure 5b). We ascribe this mode to the lowest electric system mode, in which two electric dipole moments are excited in the same direction around the vertical SRR arms. The coupling between the oscillating electric field and free electrons at the interface between ZrN and the surrounding dielectric gives rise to the confinement and enhancement of the electric field. It indicates the occurrence of an LSP resonance phenomenon in the SRRs for this mode and is the reason why it is called a plasmonic mode.[44,45] The H_z profile of Figure 5b confirms the presence of these two aligned electric dipole moments on the vertical arms of SRRs, originating from the LSP resonance. That plasmon mode is symmetric and cannot be excited upon applying a TM-polarized incident wave because it requires two identical and symmetric arms.

In agreement with other reports, the plasmon mode wavelength is shorter than the LC_0 mode and longer than LC_1 mode.[45] Moreover, the excitation of electric and magnetic modes through different input waves (TM and TE) indicates the polarization-dependent nature of SRRs. The optical response of the aforementioned simulations for the proposed ZrN SRRs fully resembles the behavior observed in other findings of Au and Ag. To further investigate, we studied the impact of geometrical parameters on the optical transmission response of ZrN SRRs. Figure 5 also shows that the LC modes underwent a redshift from 1280 to 1790 nm for LC_0 and 630 to 790 nm for LC_1 modes upon increasing the SRR size *S*. One can explain it by considering an equivalent parallel-plate capacitor and an inductor in the LC circuit. By increasing the resonator size, first, the capacitor behavior, particularly the capacitance, does not alter due to a simultaneous change in the separation distance and area of two parallel plates (vertical arms). Second, more resonator volume is exposed to the magnetic field, resulting in an enhancement in magnetic flux and consequently self-inductance of the circuit (*L*). Based on the two effects mentioned earlier and also according to the resonance equation for an LC circuit, $\lambda_{res} = 2\pi c\sqrt{LC}$, one can expect a redshift in the modal position as a result of growing size.

One can see that similar to the most used noble metals in SRRs, such as Au and Ag, the SRRs made of ZrN also exhibit the excitation of pronounced LC and plasmon modes with the capability of tailoring the optical response upon geometrical alteration. Based on our findings and according to the noticeable chemical and mechanical features of ZrN, we suggest this intermetallic compound as a material with promising optical properties with potential application in plasmonics and metamaterials devices.

3. Conclusion

In this article, we have used a series of computational approaches to investigate the plasmonic response of a transition nitride family member, ZrN, using a combination of DFT and EM modeling, including Mie theory, TMM, and FDTD methods. We showed that similar to the widely used noble metals such as Ag and Au, ZrN exhibits propagating and confined plasmonic resonances in the Kretschmann configuration and nanoparticle scattering, respectively. It also demonstrated the characteristic response of plasmonic metamaterial structures, including electric (plasmon) and magnetic modes (LC), when used in the optical SRRs. Our results showed that ZrN's plasmonic behavior appears in the visible–NIR region, exhibiting tailoring potential upon geometrical and morphological alteration. The mentioned capabilities of ZrN, along with its well-known mechanical properties, render it a promising candidate for multifunctional applications.

4. Computational Methods

4.1. DFT

We performed first-principles calculations using the DFT method as implemented in SIESTA package.[46] We used the generalized gradient approximation (GGA) in the Perdew, Burke, Ernzerhof (PBE) form to the exchange–correlation functional based on the linear combination of atomic orbital (LCAO) techniques.[47] We used a double-zeta plus polarization (DZP) orbital basis set for the real-space grid. We conducted the integration in the first Brillouin zone upon a Monkhorst–Pack[48] grid of $15 \times 15 \times 15$ along with a mesh cutoff of 300 Ry to expand electron wave functions (charges). For the structural optimization, we considered ZrN in a Rocksalt crystal structure

(shown in Figure 1a) with cell parameters of $a = b = c =$ 4.57 nm based on the experimental data, which contains four Zr and N atoms in the unit cell.[27] The relaxation process for both lattice constant and atomic position continued until the maximum force on every atom and convergence threshold for self-consistent iterations reached to less than $0.03\,\mathrm{eV\,Å^{-1}}$ and $10^{-4}\,\mathrm{eV\,atom^{-1}}$, respectively.

4.2. TMM Calculations

We used an in-house TMM code for multilayer setups to calculate the reflection and absorption of ZrN. In the setup, a 50 nm-thick ZrN layer is sandwiched between a 500 nm-thick SiO ($n = 1.52$) and a 500 nm-thick air ($n = 1$) layer. To generate the dispersion diagrams (Figure 4), we used a polychromatic plane wave, with $300 - 800$ nm wavelength range, incident through the SiO_2 medium. The incident wave impinges under an angle range of 40°–50°, with respect to the ZrN surface normal, polarized within the plane of incidence (TM), to allow for the generation of surface plasmons at the ZrN-dielectric interfaces.

4.3. FDTD Calculations

We performed the optical FDTD simulations with the commercially available OptiWave package. The ZrN SRRs comprise a varying size of S (defining the supporting square side length; see inset in Figure 5), the periodic lattice constant $a = 1.75S$, kept constant relative to S in all simulations, and the constant SRR height of 20 nm. The SRR legs have a constant width of 20 nm, while the base has a constant width of 25 nm. We used a Gaussian modulated sinusoidal EM plane wave with time offset 4×10^{-15} s and half-width 0.8×10^{-15} s to irradiate the proposed configuration. The excitation beam propagates along the vertical axis, normal to the SRR plane, with polarization parallel (TM) or perpendicular (TE) to the SRR arms (indicated as green arrows in the insets in Figure 5). The simulation unit cell is sandwiched between periodic boundary conditions in the lateral (x and y) directions and perfectly matched layers in the vertical direction. Moreover, we chose a uniform mesh size of 4 nm along the x-, y-, and z-axes after ensuring convergence and stability for the chosen setup.

Supporting Information

Supporting Information is available from the Wiley Online Library or from the author.

Acknowledgements

This work was partially financed by Interreg Deutschland-Danmark with money from the European Regional Development Fund, project numbers 086-1.1-17 (CheckNano) and 096-1.1-18 (Access & Acceleration). The computational calculations contributing to this work were conducted with support of the UCloud Services provided by the eScience Center at SDU.

Conflict of Interest

The authors declare no conflict of interest.

Data Availability Statement

Research data are not shared.

Keywords

density functional theory, electromagnetic modeling, metamaterial, optical constants, plasmonics, zirconium nitride

Received: June 21, 2021
Revised: July 14, 2021
Published online:

[1] P. West, S. Ishii, G. Naik, N. Emani, V. Shalaev, A. Boltasseva, *Laser Photon. Rev.* **2010**, *4*, 795.
[2] G. V. Naik, V. M. Shalaev, A. Boltasseva, *Adv. Mater.* **2013**, *25*, 3264.
[3] L. Yau, C. Sah, *Appl. Phys. Lett.* **1972**, *21*, 157.
[4] G. Bemski, *Phys. Rev.* **1958**, *111*, 1515.
[5] J. Zhao, S. Cao, C. Liao, Y. Wang, G. Wang, X. Xu, C. Fu, G. Xu, J. Lian, Y. Wang, *Sens. Actuat. B: Chem.* **2016**, *230*, 206.
[6] X. Cao, J. Zhou, H. Wang, S. Li, W. Wang, G. Qin, *J. Mater. Chem. A* **2019**, *7*, 10980.
[7] A. Boltasseva, *MRS Bull.* **2014**, *39*, 461.
[8] A. Boltasseva, H. A. Atwater, *Science* **2011**, *331*, 290.
[9] G. V. Naik, J. Kim, A. Boltasseva, *Opt. Mater. Express* **2011**, *1*, 1090.
[10] A. Shabani, N. Rahmani, M. K. Nezhad, *J. Electromagn. Waves Appl.* **2020**, *34*, 1372.
[11] J. B. Khurgin, A. Boltasseva, *MRS Bull.* **2012**, *37*, 768.
[12] M. Kumar, N. Umezawa, S. Ishii, T. Nagao, *ACS Photon.* **2016**, *3*, 43.
[13] A. Shabani, M. R. Roknabadi, M. Behdani, M. K. Nezhad, N. Rahmani, *J. Nanophoton.* **2017**, *11*, 1.
[14] J. Kim, G. V. Naik, A. V. Gavrilenko, K. Dondapati, V. I. Gavrilenko, S. M. Prokes, O. J. Glembocki, V. M. Shalaev, A. Boltasseva, *Phys. Rev. X* **2013**, *3*, 041037.
[15] A. Calzolari, A. Ruini, A. Catellani, *ACS Photon.* **2014**, *1*, 703.
[16] P. Patsalas, N. Kalfagiannis, S. Kassavetis, G. Abadias, D. Bellas, C. Lekka, E. Lidorikis, *Mater. Sci. Eng. R Rep.* **2018**, *123*, 1.
[17] U. Guler, V. M. Shalaev, A. Boltasseva, *Mater. Today* **2015**, *18*, 227.
[18] U. Guler, G. V. Naik, A. Boltasseva, V. M. Shalaev, A. V. Kildishev, *Appl. Phys. B* **2012**, *107*, 285.
[19] M. B. Cortie, J. Giddings, A. Dowd, *Nanotechnology* **2010**, *21*, 115201.
[20] P. Patsalas, N. Kalfagiannis, S. Kassavetis, *Materials* **2015**, *8*, 3128.
[21] A. Shabani, M. K. Nezhad, N. Rahmani, M. R. Roknabadi, M. Behdani, B. Sanyal, *Plasmonics* **2019**, *14*, 1871.
[22] A. Catellani, A. Calzolari, *Phys. Rev. B* **2017**, *95*, 115145.
[23] J. Kim, S.-H. Jhi, K. Ryeol Lee, *J. Appl. Phys.* **2011**, *110*, 083501.
[24] P. Patsalas, *Thin Solid Films* **2019**, *688*, 137438.
[25] Y. Ran, H. Lu, S. Zhao, L. Jia, Q. Guo, C. Gao, Z. Jiang, Z. Wang, *Appl. Surf. Sci.* **2019**, *476*, 560.
[26] H. Lu, Y. Ran, S. Zhao, L. Jia, C. Gao, Q. Guo, Z. Jiang, F. Yang, Z. Wang, *J. Phys. D Appl. Phys.* **2019**, *52*, 245102.
[27] Y. Gu, F. Guo, Y. Qian, H. Zheng, Z. Yang, *Mater. Lett.* **2003**, *57*, 1679.
[28] K. Aigner, W. Lengauer, D. Rafaja, P. Ettmayer, *J. Alloys Compd.* **1994**, *215*, 121.
[29] C. Stampfl, W. Mannstadt, R. Asahi, A. J. Freeman, *Phys. Rev. B* **2001**, *63*, 155106.
[30] A. Shabani, M. K. Nezhad, N. Rahmani, Y. K. Mishra, B. Sanyal, J. Adam, *Adv. Photon. Res.* **2020**, 2000086.
[31] P. Drude, *Annal. Phys.* **1900**, *308*, 369.

[32] G. Mie, *Annal. Phys.* **1908**, *330*, 377.
[33] U. Guler, S. Suslov, A. V. Kildishev, A. Boltasseva, V. M. Shalaev, *Nanophotonics* **2015**, *4*, 269.
[34] P. B. Johnson, R. W. Christy, *Phys. Rev. B* **1972**, *6*, 4370.
[35] A. Lalisse, G. Tessier, J. Plain, G. Baffou, *Sci. Rep.* **2016**, *6*, 38647.
[36] A. Nisha, P. Maheswari, P. M. Anbarasan, K. B. Rajesh, Z. Jaroszewicz, *Opt. Quantum Electron.* **2019**, *51*, 19.
[37] A. P. Vinogradov, A. V. Dorofeenko, A. A. Pukhov, A. A. Lisyansky, *Phys. Rev. B* **2018**, *97*, 235407.
[38] Y. Tang, X. Zeng, J. Liang, *J. Chem. Ed.* **2010**, *87*, 742.
[39] L. Y. M. Tobing, L. Tjahjana, D. H. Zhang, Q. Zhang, Q. Xiong, *Adv. Opt. Mater.* **2014**, *2*, 280.
[40] L. Y. M. Tobing, Y. Luo, K. S. Low, D. Zhang, D. H. Zhang, *Adv. Opt. Mater.* **2016**, *4*, 1047.
[41] B. Lahiri, S. G. McMeekin, A. Z. Khokhar, R. M. D. L. Rue, N. P. Johnson, *Opt. Express* **2010**, *18*, 3210.
[42] T. D. Corrigan, P. W. Kolb, A. B. Sushkov, H. D. Drew, D. C. Schmadel, R. J. Phaneuf, *Opt. Express* **2008**, *16*, 19850.
[43] S. Xiao, T. Wang, Y. Liu, X. Han, X. Yan, *Plasmonics* **2017**, *12*, 185.
[44] S. A. Gregory, Y. Wang, C. de Groot, O. L. Muskens, *ACS Photonics* **2015**, *2*, 606.
[45] L. Y. M. Tobing, L. Tjahjana, D. H. Zhang, Q. Zhang, Q. Xiong, *Sci. Rep.* **2013**, *3*, 2437.
[46] J. M. Soler, E. Artacho, J. D. Gale, A. Garca, J. Junquera, P. Ordejón, D. Sánchez-Portal, *J. Phys. Condens. Matter* **2002**, *14*, 2745.
[47] J. P. Perdew, K. Burke, M. Ernzerhof, *Phys. Rev. Lett.* **1996**, *77*, 3865.
[48] H. J. Monkhorst, J. D. Pack, *Phys. Rev. B* **1976**, *13*, 5188.